Supporting Information

Rattling Induced Bonding Hierarchy in Li-Cu-Ti Chalcotitanates for Enhanced Thermoelectric Efficiency: A Machine Learning Potential Approach

Harpriya Minhas,[†] Sandeep Das,[†] Rahul Kumar Sharma,[†] Biswarup Pathak[†,*]

[†] Department of Chemistry, Indian Institute of Technology (IIT) Indore, Indore, Madhya Pradesh, 453552, India

*E-mail: biswarup@iiti.ac.in

Contents

Figure S1. Convergence of the lattice thermal conductivity of $LiCu_3TiQ_4$ (Q = S, Se, and Te) against q-point mesh at 300 K. Lattice thermal conductivities are converged to 0.01 $Wm^{-1}K^{-1}$ at 17 × 17 × 17 q-point mesh.

Table S1. The sum of covalent and ionic radii (Å) of respective atoms in Ti–Q, Li–Q, and Cu–Q (Q = S, Se, or Te) and the actual bond lengths are defined in blue color.

Text S1: Thermal Stability

Figure S2. The Li-Cu-Ti-Q (Q = S, Se, or Te) quaternary phase diagram from the OQMD database. The green circles correspond to the stable phases on the energy above the convex hull (<0.25 eV/atom) for (a) $LiCu_3TiS_4$, (b) $LiCu_3TiSe_4$, and (c) $LiCu_3TiTe_4$.

Figure S3. The total electronic charge distribution contour plots for (a) $LiCu_3TiS_4$, (b) $LiCu_3TiSe_4$ along (1 -1 0) plane, and (c) $LiCu_3TiTe_4$ along (-1 -1 0) plane.

Figure S4. The position of Li in (a) $LiCu_3TiS_4$, (b) $LiCu_3TiSe_4$, and (c) $LiCu_3TiTe_4$.

Table S2: The calculated Young's modulus (GPa), shear modulus (GPa), Poisson's ratio, and Debye Temperature, θ_D (K) for the considered structures of $LiCu_3TiQ_4$.

Table S3: Energy convergence test for the considered systems.

Figure S5. The phonon dispersion relations in $LiCu_3TiTe_4$, reflecting the avoided crossing between LA acoustic and optical branch at 1.6 THz of frequency.

Text S2: Grüneisen parameter (γ)

Text S3: Weighted Phase Space

Figure S6. Boundary and isotopic scattering rates of **(a)** $LiCu_3TiS_4$, **(b)** $LiCu_3TiSe_4$, **(c)** $LiCu_3TiTe_4$ with respect to frequency (THz) at 300K.

Table S4: Calculated bandgaps using different functionals of $LiCu_3TiQ_4$ systems.

Text S4. Effective Mass

Text S5. Carrier Transport Model: Solution to the Boltzmann transport equation

Figure S7. Scattering rates as a function of energy of n-type for **(a, d)** $LiCu_3TiS_4$, **(b, e)** $LiCu_3TiSe_4$, and **(c, f)** $LiCu_3TiTe_4$. These represent their scattering mechanisms including polar optical phonon (POP), ionized impurity (IMP), and acoustic deformation potential (ADP) scattering at carrier concentrations of 10^{20} cm^{-3} at 300 K and 900 K for n-type conduction.

Figure S8. Scattering rates as a function of energy of p-type for **(a, d)** $LiCu_3TiS_4$, **(b, e)** $LiCu_3TiSe_4$, and **(c, f)** $LiCu_3TiTe_4$. These represent their scattering mechanisms including polar optical phonon (POP), ionized impurity (IMP), and acoustic deformation potential (ADP) scattering at carrier concentrations of 10^{20} cm^{-3} at 300 K and 900 K for p-type conduction.

Figure S9. Mobility (cm^2/Vs) as a function of temperature for n- and p-type doping of **(a, d)** $LiCu_3TiS_4$, **(b, e)** $LiCu_3TiSe_4$, and **(c, f)** $LiCu_3TiTe_4$ under three scattering mechanisms such as polar optical phonon (POP), ionized impurity (IMP), and acoustic deformation potential (ADP) Scattering with carrier concentrations of 10^{20} cm^{-3}.

Figure S10. The calculated electronic transport properties including electrical conductivity (S/m), Seebeck coefficient (μV/K), and electronic thermal conductivity ($Wm^{-1}K^{-1}$) for (a) $LiCu_3TiS_4$, (b) $LiCu_3TiSe_4$, and (c) $LiCu_3TiTe_4$.

Figure S11. The evaluated thermoelectric properties for $LiCu_3TiQ_4$ (Q = S, Se, or Te) **(a)** Seebeck coefficient (S), **(b)** electrical conductivity (σ), **(c)** power factor (PF), and **(d)** thermoelectric figure of merit (ZT), calculated based on relaxation times obtained transport coefficients using AMSET at carrier concentration of 10^{20} cm^{-3}. The negative and positive signs of the carrier concentrations represent n- and p-type doping.
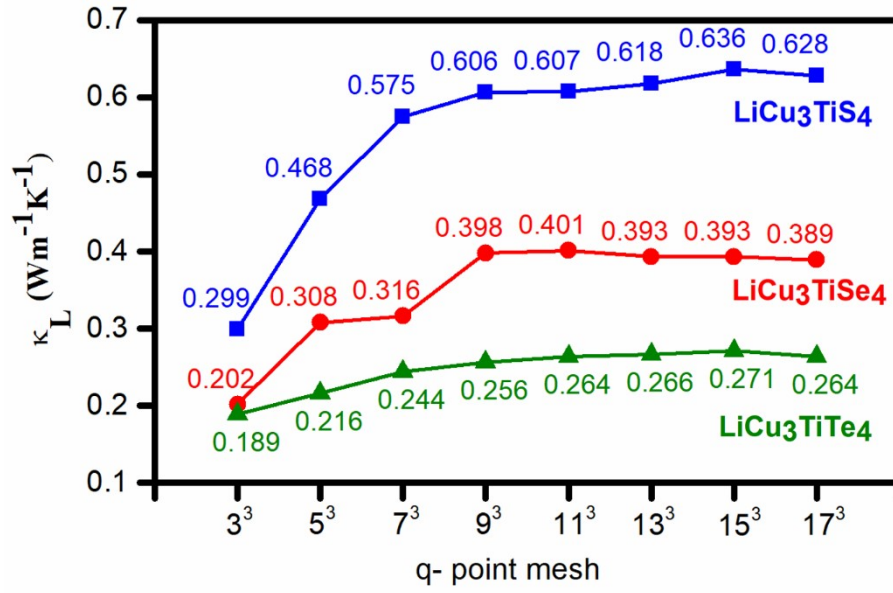
Figure S1. Convergence of the lattice thermal conductivity of $LiCu_3TiQ_4$ (Q = S, Se, and Te) against q-point mesh at 300 K. Lattice thermal conductivities are found to converge at 17 × 17 × 17 q-point mesh.

Table S1. The sum of covalent and ionic radii (Å) of respective atoms in Ti–Q, Li–Q, and Cu–Q (Q = S, Se, or Te) and the actual bond lengths are defined in blue color.

Q	Ti–Q (Å)			Li–Q (Å)			Cu–Q (Å)		
	Actual	Covalent	Ionic	Actual	Covalent	Ionic	Actual	Covalent	Ionic
S	2.29	2.36	2.52	2.48	2.32	2.60	2.35	2.32	2.80
Se	2.40	2.48	2.66	2.54	2.34	2.74	2.45	2.44	2.94
Te	2.66	2.69	2.89	2.83	2.65	2.97	2.68	2.65	3.17

Text S1: Thermal Stability

We have analyzed the Li-Cu-Ti-Q quaternary convex hull using the phase diagram creation tool in Open Quantum Materials Database (OQMD).[1-3] We have also analyzed the formation energies of these materials (LiCu3TiS4, LiCu3TiSe4, and LiCu3TiTe4) using the same tool. From the quaternary phase diagrams for Li-Cu-Ti-Q our considered systems are found to be thermodynamically stable.
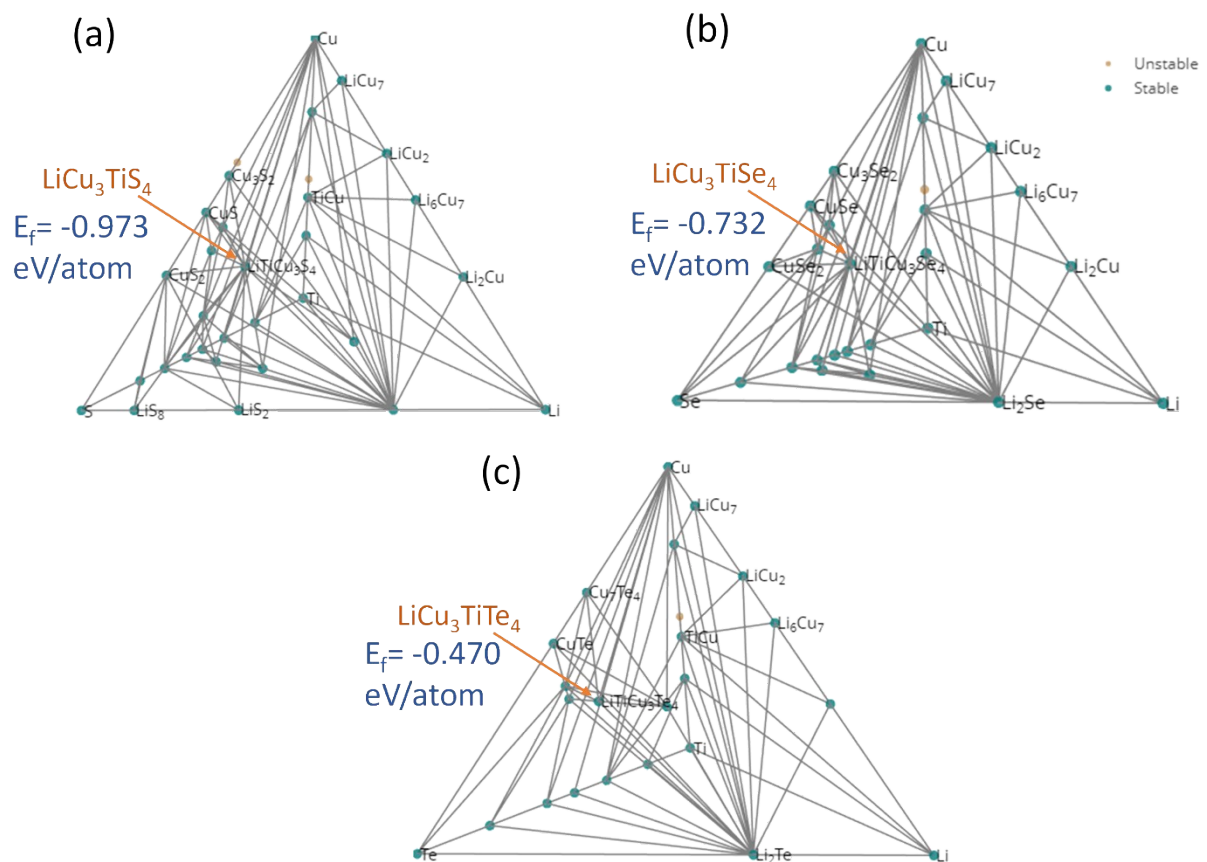

Figure S2. The Li-Cu-Ti-Q (Q = S, Se, or Te) quaternary phase diagram from the OQMD database. The green circles correspond to the stable phases on the energy above the convex hull (<0.25 eV/atom) for (a) $LiCu_3TiS_4$, (b) $LiCu_3TiSe_4$, and (c) $LiCu_3TiTe_4$.

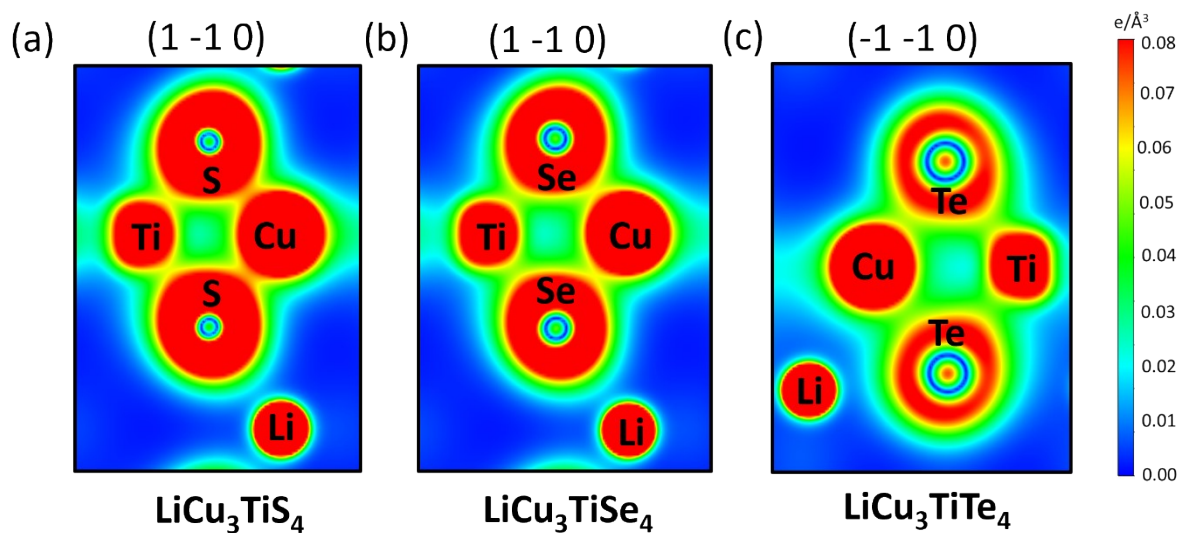**Figure S3.** The total electronic charge distribution contour plots for (a) $LiCu_3TiS_4$, (b) $LiCu_3TiSe_4$ along (1 -1 0) plane, and (c) $LiCu_3TiTe_4$ along (-1 -1 0) plane.
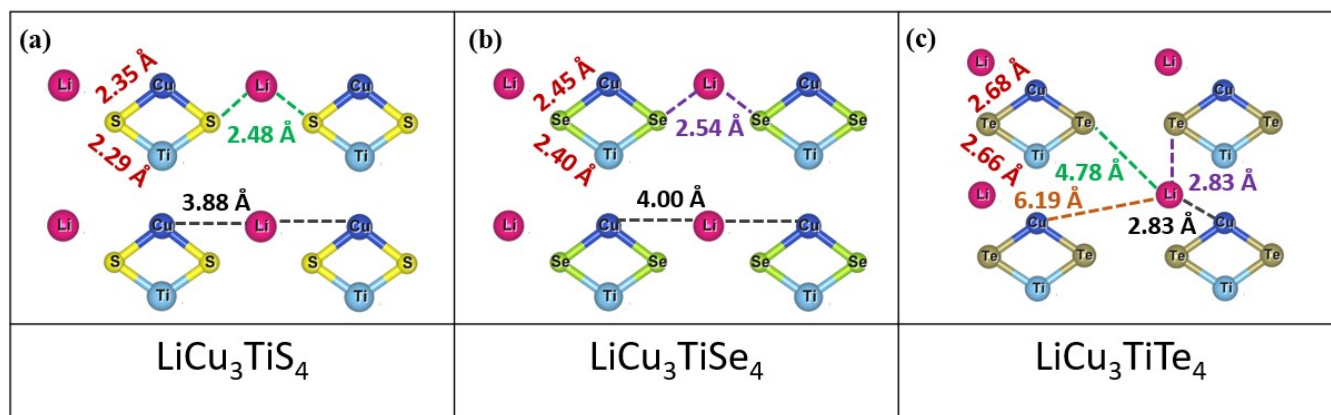
Figure S4. The position of Li in (a) $LiCu_3TiS_4$, (b) $LiCu_3TiSe_4$, and (c) $LiCu_3TiTe_4$.

Table S2: The calculated Young's modulus (GPa), shear modulus (GPa), Poisson's ratio, and Debye Temperature, θ_D (K) for the considered structures of $LiCu_3TiQ_4$.

Materials	Young's modulus	Shear modulus	Poisson's ratio	θ_D
$LiCu_3TiS_4$	78.62	31.036	0.38	338
$LiCu_3TiSe_4$	59.88	22.54	0.22	240
$LiCu_3TiTe_4$	30.58	11.8	0.39	157

Table S3. Energy convergence test for the considered systems.

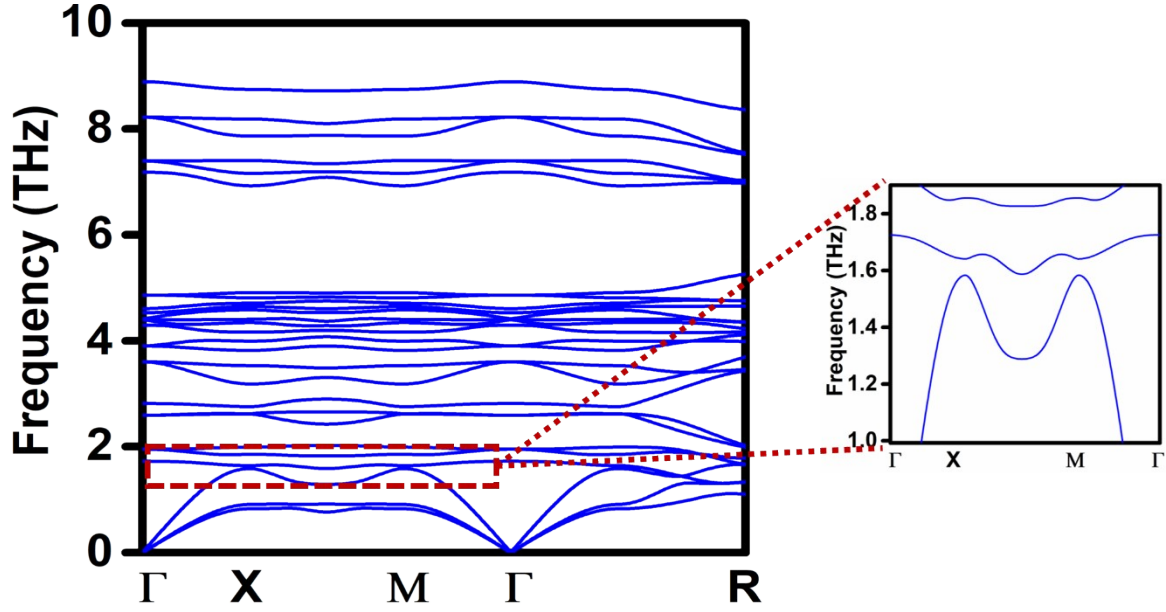| Energy cutoff (eV)	Total Energy (eV)		
	$LiCu_3TiS_4$	$LiCu_3TiSe_4$	$LiCu_3TiTe_4$
400	-46.95	-43.34	-34.88
450	-46.92	-43.31	-34.84
500	-46.92	-43.31	-34.84
550	-46.92	-43.31	-34.86
600	-46.92	-43.31	-34.84
650	-46.92	-43.31	-34.84
700	-46.92	-43.31	-34.85

Figure S5. The phonon dispersion relations in LiCu$_3$TiTe$_4$, reflect the avoided crossing between LA acoustic and optical branch at 1.6 THz of frequency.

Text S2: Grüneisen parameter (γ)

The quantify the anharmonicity within the periodic crystals, we have calculated the Grüneisen parameter (γ) defined as,

$$\gamma = \frac{- d\ln \omega_q}{d\ln V} \tag{S1}$$

where ω_q and V represents the phonon frequencies and volume, respectively.

Text S3: Weighted Phase Space

The weighted phase space (W^{total}_q) is evaluated which is obtained from the following equation,[50]

$$P^{\pm}_q = \frac{1}{N}\sum_{q'q''}\left\{\begin{matrix} n''_q - n'_q \\ n''_q + n'_q + 1 \end{matrix}\right\}\delta\left(\omega_q - \omega'_q \pm \omega''_q\right) \qquad (S2)$$

where P^{+}_q and P^{-}_q denotes the energy and momentum conserved scattering phase spaces for phonon mode q in the absorption (+) and emission (-) processes, where the summation is restricted to the pairs (q_1, q_2) satisfying $q + q_1 + q_2 = G$, where G is the inverse lattice vector.
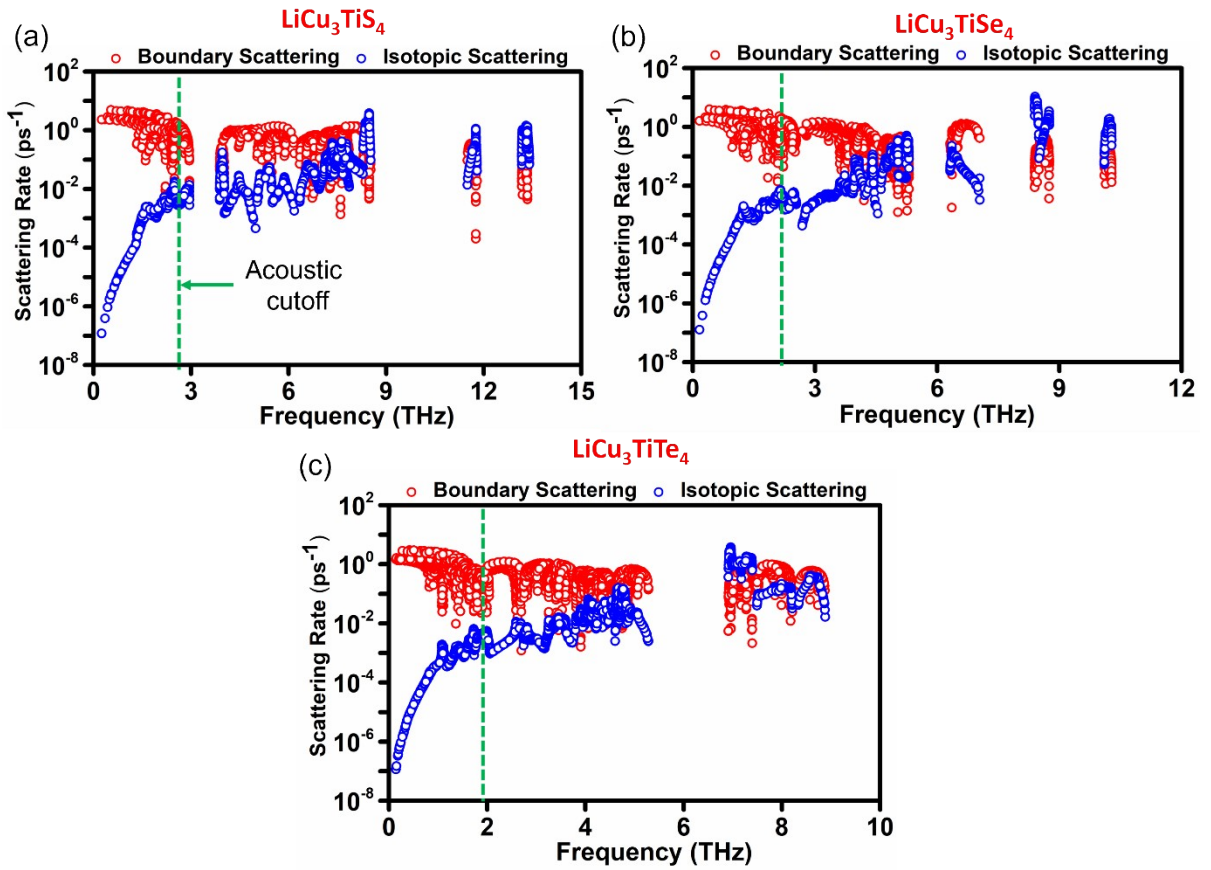

Figure S6. Boundary and isotopic scattering rates of **(a)** LiCu$_3$TiS$_4$, **(b)** LiCu$_3$TiSe$_4$, **(c)** LiCu$_3$TiTe$_4$ with respect to frequency (THz) at 300K.

Table S4: Calculated bandgaps using different functionals for $LiCu_3TiQ_4$ systems.

Functional	$LiCu_3TiS_4$	$LiCu_3TiSe_4$	$LiCu_3TiTe_4$
PBE	1.52	1.25	1.11
HSE06 (25%)	3.50	3.20	2.30
HSE06 (20%)	3.16	2.83	2.19
HSE06 (10%)	2.32	2.02	2.38
HSE06 (5%)	1.92	1.64	1.43
HSE03 (25%)	3.30	2.97	2.15
HSE03 (20%)	2.94	2.62	2.03
HSE03 (10%)	**2.22**	**1.92**	1.63
HSE03 (5%)	1.86	1.59	**1.39**
MBJ	1.52	1.31	1.22
SCAN	1.67	1.44	1.32
SCAN_RPR	1.67	1.44	1.32
SCAN_rVV10	1.73	1.50	1.36
Exp[4]	**2.3**	**1.86**	**1.34**

Text S4. Effective Mass

The effective mass is associated with the formula:

$$m^* = \hbar^2 \left(\frac{d^2 E}{dk_i dk_j} \right)^{-1}$$

(S3)

where E and k represents the energy and wave vector.

Text S5. Carrier Transport Model: Solution to the Boltzmann Transport Equation

The general form of the electron distribution remains the equilibrium Fermi-Dirac distribution is written as:

$$f(k) = f_0[\in (k)] + xg(k) \tag{S4}$$

where f is the actual distribution of the electrons, including both elastic and inelastic scattering mechanisms, f_0 is the equilibrium Fermi-Dirac distribution, x is the cosine of the angle between the small driving force and k, $g(k)$ is the perturbation to the distribution caused by the small driving force In the reformulated Boltzmann transport equation shown in Eq. (S5), there are scattering-in, $S_i(g)$, and scattering out, S_o, terms for inelastic scattering mechanisms. However, these terms also depend, in turn, on the electronic distribution as well as elastic scattering rates, v_{el}. Therefore, the BTE must be solved self-consistently to obtain $g(k)$:[5]

$$g(k) = \frac{S_i[g(k)] - v(k)\left(\dfrac{\partial f}{\partial z}\right) - \dfrac{eE}{\hbar}\left(\dfrac{\partial f}{\partial k}\right)}{S_o(k) + v_{el}(k)} \tag{S5}$$

Where E is the low electric field and $v(k)$ is the electron group velocity. The inelastic scattering mechanism that tends to dominate at room temperature is polar optical (PO) phonon scattering.

The influence of inelastic scattering mechanisms on g, and therefore the overall mobility, are captured through the terms $S_i(g)$, and S_o in Eq. (S5), while elastic scattering mechanisms affect the overall mobility by the term v_{el}. This term is the sum of all elastic scattering rates inside the material; it can be evaluated according to Matthiessen's rule:

$$v_{el}(k) = v_{ii}(k) + v_{pe}(k) + v_{de}(k) + v_{dis}(k) \tag{S6}$$

where the subscripts el, ii, pe, de, and dis stand for elastic, ionized impurity, piezoelectric, deformation potential, and dislocation scattering rates, respectively. Therefore, the effect of relevant elastic and inelastic scattering mechanisms are considered by explicitly solving the BTE [Eq. (S4)] to obtain $g(k)$.

When calculating various properties, several terms in Eq. (S2) will be set to zero. For a Seebeck coefficient, S, calculation, the applied electric driving force, $-\frac{eE}{\hbar}\left(\frac{\partial f}{\partial k}\right)$, is set to zero. Only the thermal driving force, $v(k)\left(\frac{\partial f}{\partial z}\right)$, in Eq. (S6) is taken into consideration when calculating the perturbation to the electron distribution.[6] Assuming a uniform electron concentration over the space at which a small temperature difference exists, the Seebeck coefficient is:

$$S = \frac{k_B}{e}\left[\frac{\varepsilon_F}{k_B T} - \frac{\int k^2 f(1-f)\left(\frac{\varepsilon}{k_B T}\right)dk}{\int k^2 f(1-f)dk}\right] - \frac{\frac{J}{\sigma}}{\frac{\partial T}{\partial z}}$$

(S7)

For a mobility calculation, the applied thermal driving force in Eq. (S5) is set to zero, so that only the contribution of the electric driving force is included. The mobility is:

$$\mu = \frac{1}{3}\frac{\int v(k)\left(\frac{k}{\pi}\right)^2\left(\frac{g}{E}\right)dk}{\int \left(\frac{k}{\pi}\right)^2 f dk}$$

(S8)

In Eq. (S7), the free electron density of states, $\left(\frac{k}{\pi}\right)^2$ has been used, which would limit its applicability in semiconductors. Thus, the replacement of this term by its ab initio–calculated counterpart would greatly improve the accuracy of the resulting mobility. Furthermore, the scalar group velocity, v (k), is used since the energy is averaged as a function of distance from the point. In general, we use the band structure, density of state, electron group velocity,

conduction band wave function, deformation potentials, and POP phonon frequency in calculating the mobility and Seebeck coefficient. Therefore, all the required inputs to Eq. (S8) are calculated ab initio, which greatly enhances the predictability of the model.

Once the mobilities of the electrons and holes are known, the electrical conductivity can be readily calculated:

$$\sigma = ne\mu_e + pe\mu_h \tag{S9}$$

Where, n and p, are the concentration of electrons and holes, respectively, e is the absolute value of the charge of an electron, and μ_e and μ_h are the mobility of electrons and holes respectively.
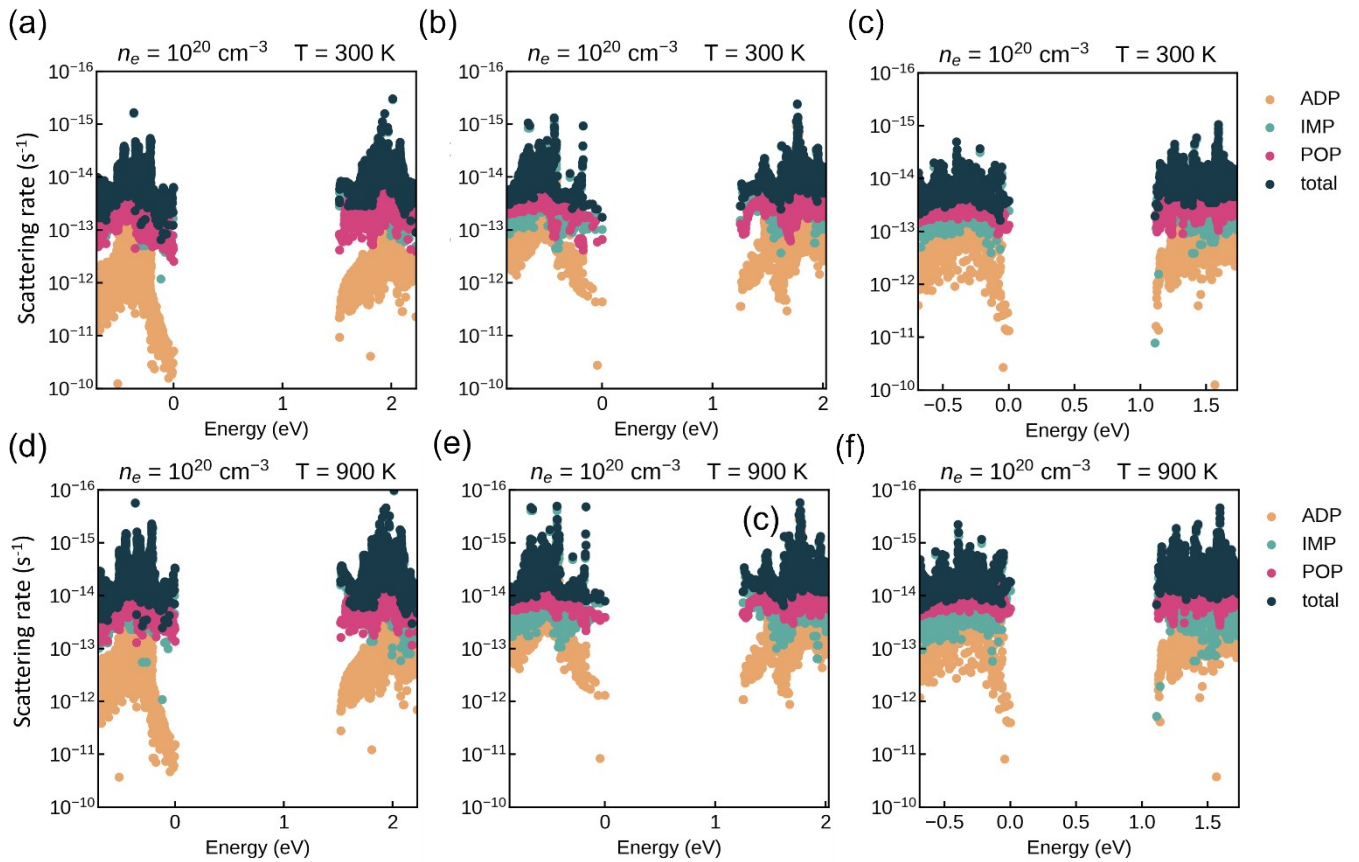
Figure S7. Scattering rates as a function of energy of n-type for **(a, d)** LiCu$_3$TiS$_4$, **(b, e)** LiCu$_3$TiSe$_4$, and **(c, f)** LiCu$_3$TiTe$_4$. These represent their scattering mechanisms including polar optical phonon (POP), ionized impurity (IMP), and acoustic deformation potential (ADP) scattering at carrier concentrations of 10^{20} cm^{-3} at 300 K and 900 K for n-type conduction.
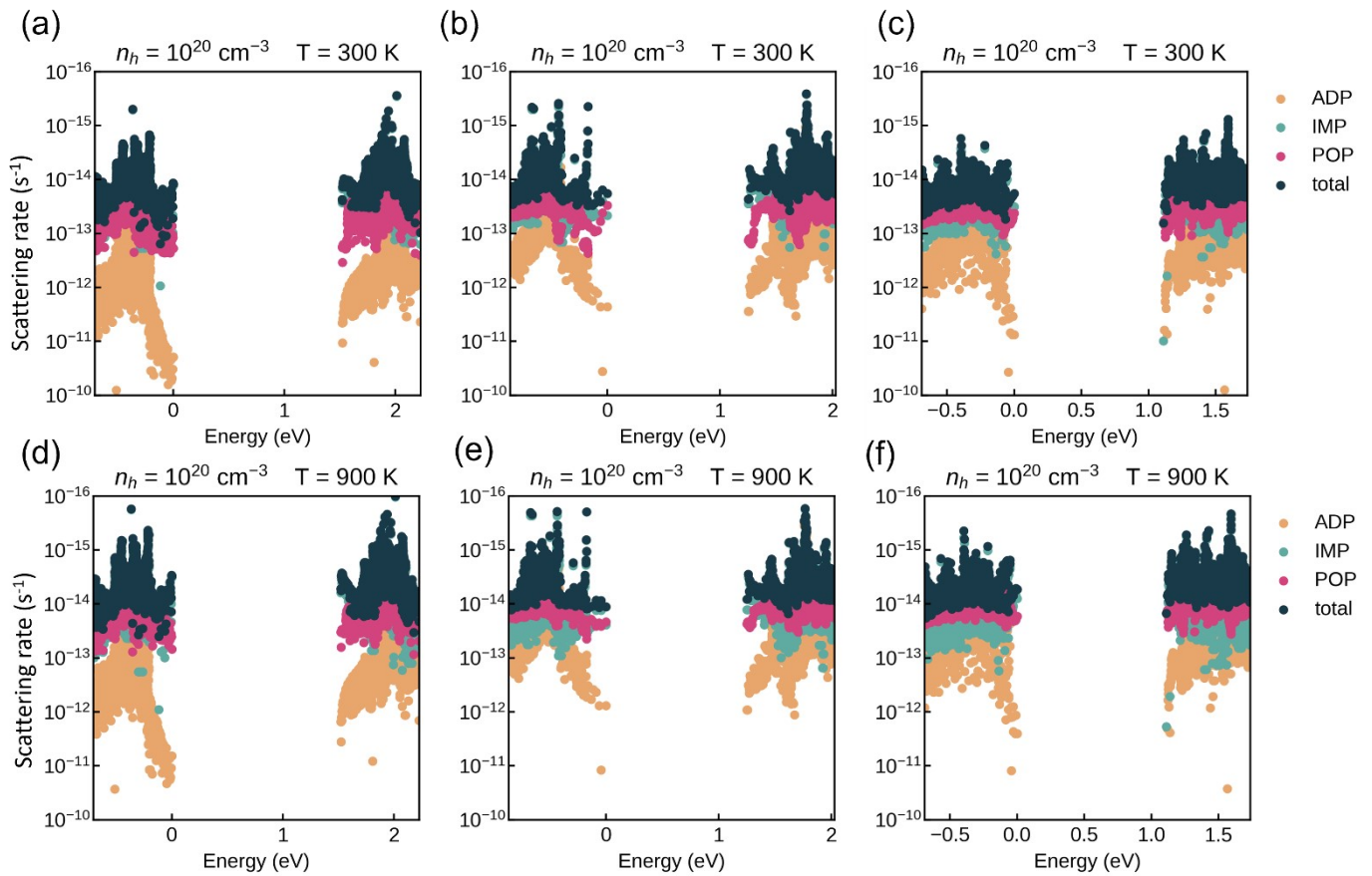

Figure S8. Scattering rates as a function of energy of p-type for **(a, d)** LiCu$_3$TiS$_4$, **(b, e)** LiCu$_3$TiSe$_4$, and **(c, f)** LiCu$_3$TiTe$_4$. These represent their scattering mechanisms including polar optical phonon (POP), ionized impurity (IMP), and acoustic deformation potential (ADP) scattering at carrier concentrations of 10^{20} cm^{-3} at 300 K and 900 K for p-type conduction.
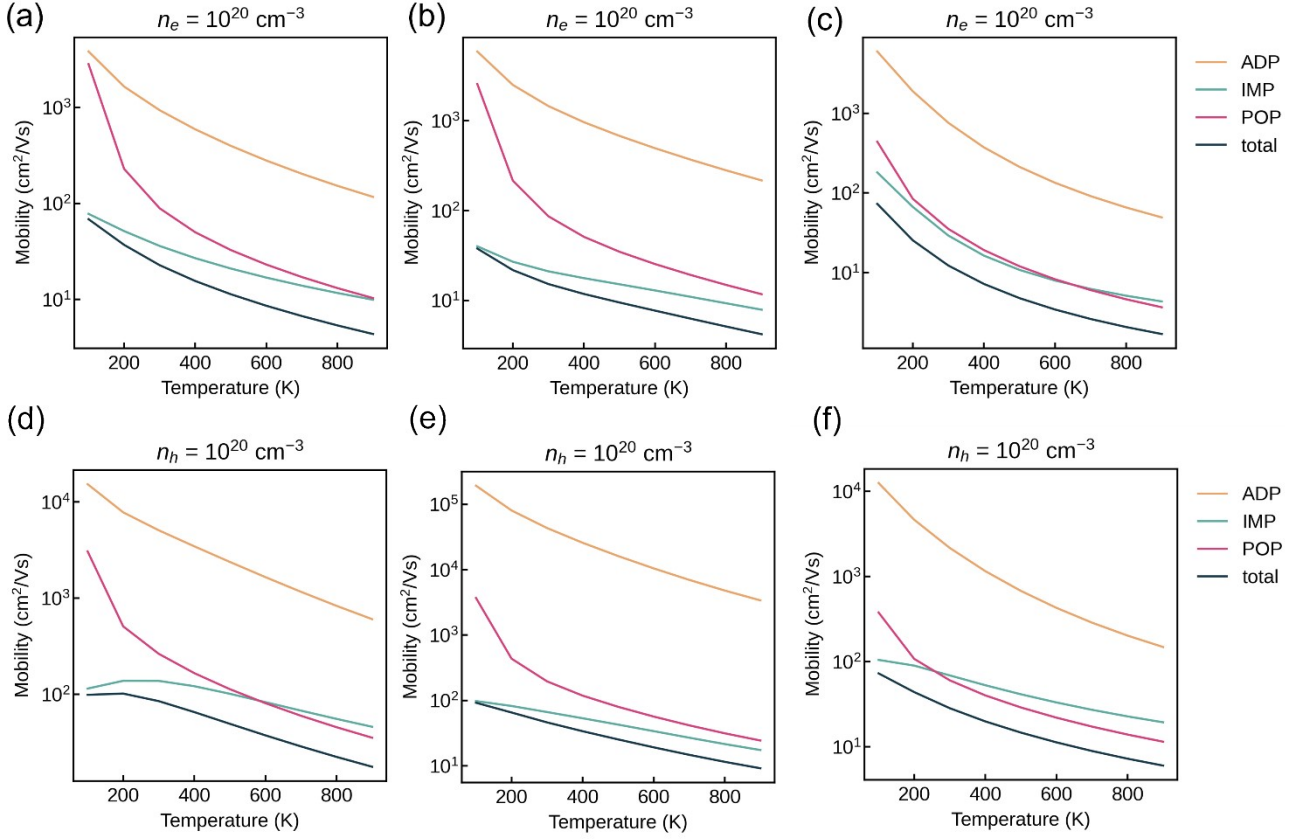
Figure S9. Mobility (cm^2/Vs) as a function of temperature for n- and p-type doping of **(a, d)** LiCu$_3$TiS$_4$, **(b, e)** LiCu$_3$TiSe$_4$, and **(c, f)** LiCu$_3$TiTe$_4$ under three scattering mechanisms namely, polar optical phonon (POP), ionized impurity (IMP), and acoustic deformation potential (ADP) scattering with carrier concentrations of 10^{20} cm^{-3}.
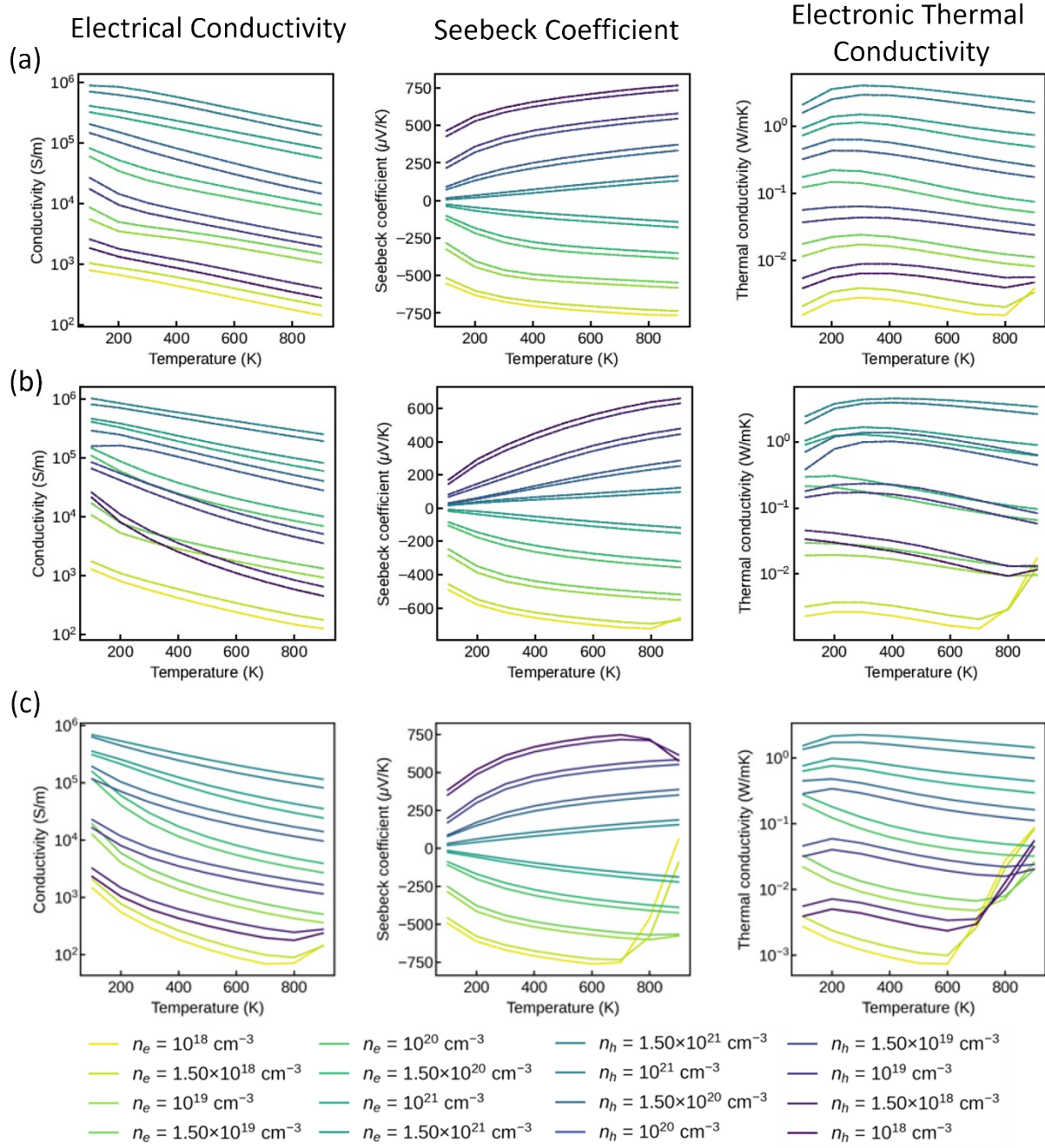
Figure S10. The calculated electronic transport properties including electrical conductivity (S/m), Seebeck coefficient (μV/K), and electronic thermal conductivity ($Wm^{-1}K^{-1}$) for (a) $LiCu_3TiS_4$, (b) $LiCu_3TiSe_4$, and (c) $LiCu_3TiTe_4$.

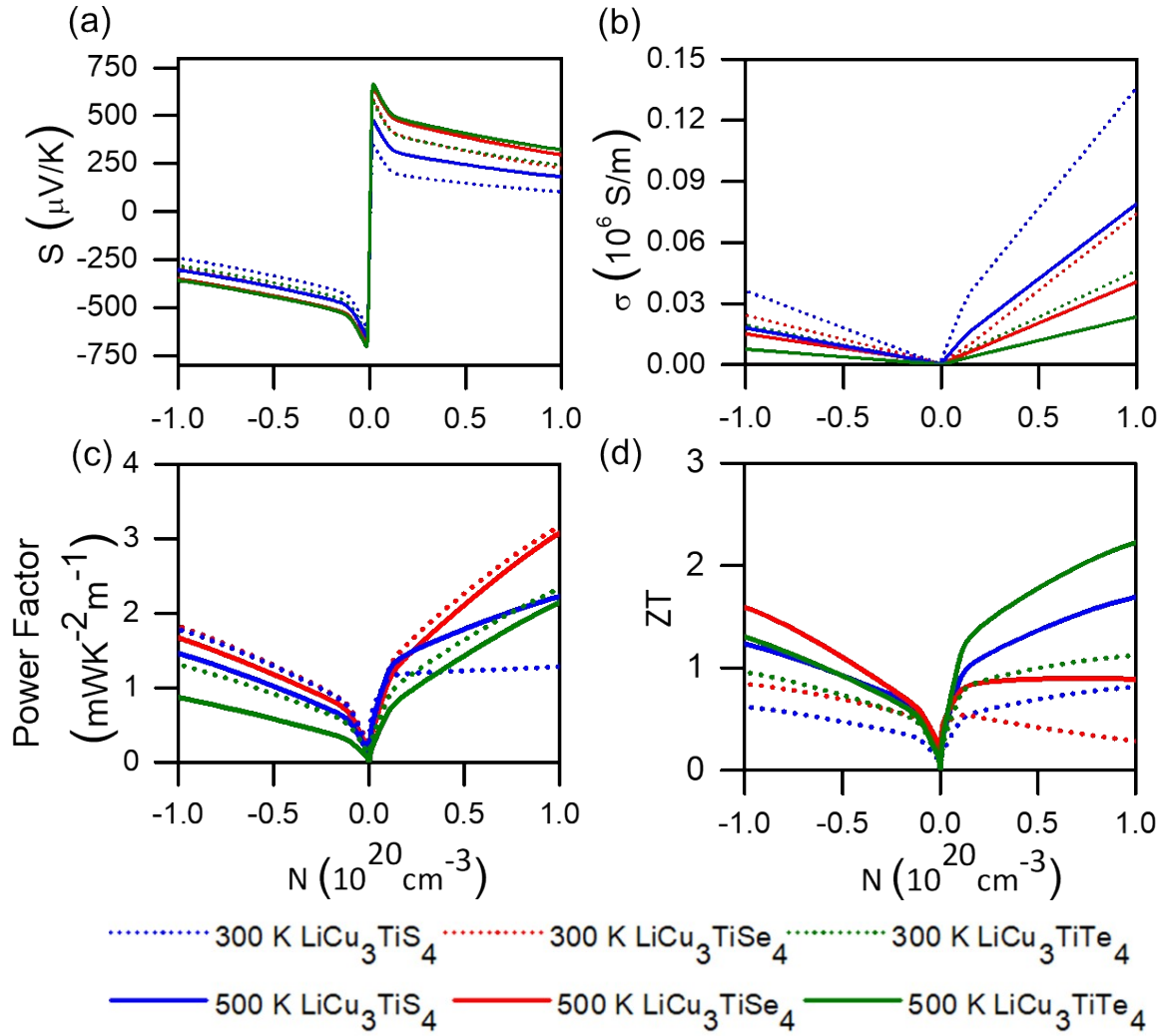**Figure S11.** The evaluated thermoelectric properties for LiCu$_3$TiQ$_4$ (Q = S, Se, or Te) **(a)** Seebeck coefficient (S), **(b)** electrical conductivity (σ), **(c)** power factor (PF), and **(d)** thermoelectric figure of merit (ZT), calculated based on relaxation times obtained transport coefficients using AMSET at carrier concentration of 10^{20} cm^{-3}. The negative and positive signs of the carrier concentrations represent n- and p-type doping.

References

1. https://www.oqmd.org/analysis/phase_diagram/

2. 1. Barber, C., Dobkin, D. & Huhdanpaa, H. *ACM Trans Math Softw*. **1996** 22, 469–483.

3. 2. Stevanović, V., Lany, S., Zhang, X. & Zunger, A. *Phys. Rev. B* **2012**, 85, 115104

4. M. A.Quintero, J. Shen, C. C. Laing, C.Wolverton, and M. G.Kanatzidis *J. Am. Chem. Soc.* **2022**, *144*(28).

5. A.Faghaninia, J. W. Ager, and C. S.Lo *Phys Rev B Condens Matter Mater Phys* **2015**, *91* (23).

6. A. M.Ganose, J. Park, A. Faghaninia, R. Woods-Robinson, K. A. Persson, and A.Jain *Nat. Commun*. **2021**, *12*(1).